

Papers published in *Ocean Science Discussions* are under  
open-access review for the journal *Ocean Science*

**Sea-surface  
variability sensitivity  
to resolution**

T. Penduff et al.

# Impact of model resolution on sea-level variability characteristics at various space and time scales: insights from four DRAKKAR global simulations and the AVISO altimeter data

T. Penduff<sup>1, 2</sup>, M. Juza<sup>1</sup>, L. Brodeau<sup>1,\*</sup>, G. C. Smith<sup>3,\*\*</sup>, B. Barnier<sup>1</sup>, J.-M. Molines<sup>1</sup>,  
and A.-M. Treguier<sup>4</sup>

<sup>1</sup>Laboratoire des Ecoulements Géophysiques et Industriels, Grenoble, France

<sup>2</sup>Dept. of Oceanography, Florida State University, USA

<sup>3</sup>National Oceanography Centre, Southampton, UK

Title Page

Abstract

Introduction

Conclusions

References

Tables

Figures

⏪

⏩

◀

▶

Back

Close

Full Screen / Esc

Printer-friendly Version

Interactive Discussion



<sup>4</sup>Laboratoire de Physique des Océans, Brest, France

\*now at: Department of Meteorology, Stockholm University, Sweden

\*\*now at: Northwest Atlantic Fisheries Centre, Fisheries and Ocean Canada, Canada

Received: 1 June 2009 – Accepted: 16 June 2009 – Published: 8 July 2009

Correspondence to: T. Penduff (thierry.penduff@legi.grenoble-inp.fr)

Published by Copernicus Publications on behalf of the European Geosciences Union.

**OSD**

6, 1513–1545, 2009

---

**Sea-surface  
variability sensitivity  
to resolution**

T. Penduff et al.

---

Title Page

Abstract

Introduction

Conclusions

References

Tables

Figures

◀

▶

◀

▶

Back

Close

Full Screen / Esc

Printer-friendly Version

Interactive Discussion



## Abstract

Four global ocean/sea-ice simulations driven by the same realistic 46-year daily atmospheric forcing were performed within the DRAKKAR project at  $2^\circ$ ,  $1^\circ$ ,  $\frac{1}{2}^\circ$ , and  $\frac{1}{4}^\circ$  resolutions. Model sea-level anomalies are collocated over the period 1993–2004 onto the AVISO SLA dataset. These five collocated SLA datasets are then filtered and quantitatively compared over various time and space scales regarding three characteristics: SLA standard deviations, spatial correlations between SLA variability maps, and temporal correlations between observed and simulated band-passed filtered local SLA timeseries. Beyond the  $2^\circ$ – $1^\circ$  transition whose benefits are quite moderate, further increases in resolution and associated changes in subgrid scale parameterizations simultaneously induce (i) strong increases in SLA standard deviations, (ii) strong improvements in the spatial distribution of SLA variability, and (iii) slight decreases in temporal correlations between observed and simulation SLA timeseries. These 3 effects are not only clear on mesoscale (14–180 days) and quasi-annual (5–18 months) fluctuations, but also on the slower (interannual), large-scale variability ultimately involved in ocean-atmosphere coupled processes. Most SLA characteristics are monotonically affected by successive resolution increases, but irregularly and with a strong dependence on frequency and latitude. Benefits of enhanced resolution are maximum in the  $\frac{1}{2}^\circ$ – $\frac{1}{4}^\circ$  transition, in the 14–180 day range, and within eddy-active mid- and high-latitude regions. They are particularly clear in the Southern Ocean where mesoscale eddies probably sustain a substantial intrinsic interannual variability.

## 1 Introduction

The choice of ocean/sea-ice primitive equation model configurations for global climate-oriented (multidecadal or longer) studies generally results from a compromise between the range of time and space scales to be simulated and the available computer resources.

OSD

6, 1513–1545, 2009

### Sea-surface variability sensitivity to resolution

T. Penduff et al.

Title Page

Abstract

Introduction

Conclusions

References

Tables

Figures

◀

▶

◀

▶

Back

Close

Full Screen / Esc

Printer-friendly Version

Interactive Discussion



**Sea-surface  
variability sensitivity  
to resolution**

T. Penduff et al.

Title Page

Abstract

Introduction

Conclusions

References

Tables

Figures

◀

▶

◀

▶

Back

Close

Full Screen / Esc

Printer-friendly Version

Interactive Discussion



Laminar ocean models ( $1^\circ$ -resolution and coarser) do not explicitly resolve mesoscale eddies and fluxes: subgrid-scale diffusive (e.g. laplacian operators) and advective (e.g. Gent and McWilliams, 1990, noted GM90 hereafter) parameterizations are used to mimick certain down-gradient eddy fluxes. Such parameterizations were not designed to mimick up-gradient fluxes though, nor the inverse cascade fed by non-linear interactions at scales close to the first internal deformation radius (e.g. Scott and Arbic, 2007). Resolving wide western boundary currents in coarse-resolution models also requires strong viscosity values, which damp a substantial part of the currents' variability. Because they are computationally-effective, laminar oceans are being used in most global coupled models to address paleoclimatic and prediction issues (i.e. IPCC).

“Eddy-admitting” ocean models (roughly  $\frac{1}{2}^\circ$  to  $\frac{1}{10}^\circ$  resolution) resolve mesoscale eddies where the local ratio between the grid scale and dynamically-unstable scales is small enough. Parameterizations are also used at these resolutions to represent unresolved downgradient eddy fluxes, but through more scale-selective (often bilaplacian) operators able to preserve the resolved part of the mesoscale spectrum. Non-linear energy transfers occur at mesoscale in such models, and may then feed back onto larger space and time scales through inverse cascade or rectification processes (e.g. Zhai et al., 2004; Penduff et al., 2007).

Primitive equation models are being implemented and assessed at even higher resolution; recent studies show that they yield further dynamical improvements (e.g. Smith et al., 2000; McClean et al., 2002; Masumoto et al., 2004; Drillet et al., 2005; Treguier et al., 2005; Kelly et al., 2007; Chanut et al., 2008; Hecht and Smith, 2008; Hecht and Hasumi, 2008). Most of these simulations are presently restricted to either individual basins and/or decade-long integrations. Several years or research and computational power increase will probably be needed before these promising models can eventually be used by a wide community in long-term, forced and coupled global simulations.

The superiority of  $\frac{1}{2}^\circ$ – $\frac{1}{6}^\circ$  over laminar ocean models for large-scale ocean simulations has been demonstrated by many authors since the pioneering works by

---

**Sea-surface  
variability sensitivity  
to resolution**T. Penduff et al.

---

[Title Page](#)[Abstract](#)[Introduction](#)[Conclusions](#)[References](#)[Tables](#)[Figures](#)[Back](#)[Close](#)[Full Screen / Esc](#)[Printer-friendly Version](#)[Interactive Discussion](#)

Holland et al. (1983) and Semtner and Chervin (1988a,b), and largely confirmed since then in terms of mean states, mesoscale features, and their mutual interactions (e.g. Böning and Budich, 1992; Beckmann et al., 1994; Böning and Bryan, 1996; Dengg et al., 1996; Haidvogel et al., 2000; Gulev et al., 2007; DYNAMO Group, 1997). Eddy-admitting models are also expected to be beneficial when coupled to the atmosphere (see e.g. Fanning and Weaver, 1997), and are presently being substituted for laminar models in hindcasts or forecasts of the full climate system. Global eddy-admitting models thus presently appear as an interesting trade-off between available computer resources, the partial resolution of mesoscale effects, and the need to perform several multi-decadal integrations to study climate-related oceanic changes.

This study is focused on the comparison between laminar and eddy-admitting ocean simulations with respect to real observations. Besides the few studies mentioned above, however, the skills of eddy-admitting and laminar ocean models have not been quantitatively assessed at interannual-to-decadal timescales, at which the ocean largely controls the climate variability. The aim of this study is to quantitatively evaluate the behavior of four state-of-the-art global ocean/sea-ice simulations representative of laminar and eddy-admitting classes ( $2^\circ$  and  $1^\circ$ , and  $\frac{1}{2}^\circ$  and  $\frac{1}{4}^\circ$  resolutions, respectively) over a large range of timescales, with a special focus on interannual variability. These four ocean/sea-ice 1958–2004 hindcasts (Drakkar Group, 2007) were performed by the DRAKKAR consortium<sup>1</sup>. The AVISO altimeter dataset is chosen as a reference for its unique quasi-global character and its wide range of space-time scales, despite its restriction to the ocean surface. The present assessment is performed on atmospherically-forced models, but our complementary investigation of simulated interannual variabilities at scales larger than  $6^\circ$  may also help illustrate how increased resolution might also modify the behavior of numerical oceans in coupled mode.

Model-observation and model-model comparisons will be performed globally and locally within various frequency ranges regarding the following three criteria: magnitude and spatial distribution of the simulated SLA variability, and temporal correlations

---

<sup>1</sup><http://www.ifremer.fr/lpo/drakkar/>

between local timeseries of observed and simulated SLAs. This study also complements and extends the assessment of Drakkar simulations (e.g. Barnier et al., 2009; Treguier et al., 2007; Penduff et al., 2007) following a dedicated approach (model-observation collocation, dedicated metrics) to yield a quantitative benchmark between various classes of models.

The following section presents the four model setups, the methods used to collocate their outputs on the AVISO dataset and filter the results, the criteria and metrics used to compare them together. The effect of resolution is assessed with respect to the 3 criteria introduced above within three ranges of timescales separated by 5 and 18 months cutoff periods (Sects. 3, 4, 5). Section 6 discusses the links between resolution-induced changes on the magnitude of SLA variability, and changes in space-time correlations. In Sect. 7, the comparison of interannual variabilities will be restricted to scales larger than  $6^\circ$ , i.e. the range of scales that is resolved in the five datasets, and that is likely to be most involved in ocean atmosphere coupling.

## 2 Model configurations and assessment procedure

### 2.1 Model configurations

Our model setups are based on the NEMO code (Madec, 2008) and differ by their horizontal resolutions ( $\frac{1}{4}^\circ$ ,  $\frac{1}{2}^\circ$ ,  $1^\circ$ ,  $2^\circ$ ). Figure 1 shows that in the  $2^\circ$  and  $1^\circ$  configurations, the meridional resolution  $dy$  is increased toward the equator where it reaches  $\frac{1}{2}^\circ$  and  $\frac{1}{3}^\circ$ , respectively. The four simulations share the same vertical discretization (46 geopotential levels whose spacing progressively increase from 6 m at the surface to 250 unitm at the bottom), the same parameterization of unresolved vertical mixing and convection processes (TKE turbulent closure scheme), and surface forcing. The four runs were driven over this 47-year period by the same hybrid forcing function, described in Brodeau et al. (2006, 2009): precipitations and radiative fluxes come from satellite products; air-sea and air-ice turbulent fluxes are computed through bulk for-

## Sea-surface variability sensitivity to resolution

T. Penduff et al.

Title Page

Abstract

Introduction

Conclusions

References

Tables

Figures

◀

▶

◀

▶

Back

Close

Full Screen / Esc

Printer-friendly Version

Interactive Discussion



**Sea-surface  
variability sensitivity  
to resolution**

T. Penduff et al.

Title Page

Abstract

Introduction

Conclusions

References

Tables

Figures

◀

▶

◀

▶

Back

Close

Full Screen / Esc

Printer-friendly Version

Interactive Discussion



mulae from surface model variables and corrected 10-m atmospheric state variables from ECMWF (ERA40 reanalysed fields before 2002, ECMWF analysed fields afterwards). Uncertainties in precipitation fields, along with the need to limit drifts requires in all runs a moderate (60-day timescale over the upper 10 m, i.e. 600-day over 100 m mixed layers) relaxation of sea-surface salinity toward the monthly Levitus et al. (1998) climatology. The technical report by Molines et al. (2006) describes the parameterizations and numerical choices made in the  $\frac{1}{4}^\circ$  simulation, named ORCA025-G70. Preliminary assessments of this  $\frac{1}{4}^\circ$  simulation and physical studies may be found in e.g. Drakkar Group (2007) and Treguier et al. (2007). Timmermann et al. (2005) and Cravatte et al. (2007) provide complementary information on the  $2^\circ$  model (despite a different vertical resolution and forcing); the same  $2^\circ$  model is compared to other ocean/sea-ice components of climate models by Griffies et al. (2009).

In all runs, the bottom topography is discretized as partial steps for an accurate representation of topographic slopes and  $\frac{f}{H}$  contours. The momentum advection scheme (Arakawa and Lamb, 1981) conserves both energy and potential enstrophy. These latter two choices were shown to yield a remarkably realistic  $\frac{1}{4}^\circ$  global model solution in preliminary climatological simulations, thanks to improved numerical schemes and subsequent eddy-topography interactions (Penduff et al., 2007; Le Sommer et al., 2009). We do not expect such a benefit at coarser resolutions where weak or parameterized mesoscale turbulence cannot drive realistic topographically-rectified mean flows. The same quadratic bottom friction parameterization is used in all simulations (see Penduff et al., 2007).

Although as many numerical and physical parameters as possible (e.g. initial states, surface forcing, bulk formulae, vertical physics, bottom friction, etc.) were kept identical in the four configurations, certain parameters needed to be adjusted according to the numerical and physical specificity of each configuration, in order to yield the most consistent and realistic solution in their specific dynamical regimes. In both eddy-admitting simulations, temperature and salinities are mixed along isopycnals through a laplacian operator; the associated diffusion coefficients at the equator equal 300 and 600  $\text{m}^2 \text{s}^{-1}$

## Sea-surface variability sensitivity to resolution

T. Penduff et al.

Title Page

Abstract

Introduction

Conclusions

References

Tables

Figures

◀

▶

◀

▶

Back

Close

Full Screen / Esc

Printer-friendly Version

Interactive Discussion



in the  $\frac{1}{4}^\circ$  and  $\frac{1}{2}^\circ$  models respectively, and decrease proportionally to the grid size. Horizontal viscosity is achieved by bilaplacian operators at  $\frac{1}{4}^\circ$  and  $\frac{1}{2}^\circ$  resolutions; associated coefficients at the equator equal  $1.5 \times 10^{11}$  and  $12 \times 10^{11} \text{ m}^4 \text{ s}^{-1}$  respectively, and vary as the cube of the gridsize. A free-slip sidewall boundary condition is used in the  $\frac{1}{4}^\circ$  and  $\frac{1}{2}^\circ$  models.

Mesoscale eddies are absent in both laminar configurations: the isopycnal laplacian tracer mixing is complemented by a GM90 parameterization, and momentum mixing is performed by a horizontal laplacian operator. Details about the spatial distribution of the associated coefficients may be found in Cravatte et al. (2007) for the  $2^\circ$  model; these coefficients were simply divided by two in the  $1^\circ$  simulation. The sidewall boundary condition is free-slip at  $1^\circ$  resolution, but no-slip at  $2^\circ$  resolution, as is usually done in climate-oriented simulations with this configuration.

All simulation outputs are started from rest in 1958 on the first of January, and are archived on their native grids over the 47-year (1958–2004) model runs as successive 5-day averages labeled by the central date (e.g. the 5-day average between January first and fifth is dated January third at noon). The present study focuses on the last 12 years (1993–2004) when altimeter observations are available, thus ensuring in the four integrations a relatively long (35-year) and identical period of spinup.

## 2.2 Model-observation and model-model comparison methodology

### 2.2.1 Collocation and filtering

Simulated SSH 5-day averages are first linearly interpolated in time and space at the resolution of observed SLA fields (weekly and on a  $1/3^\circ \times 1/3^\circ$  Mercator grid) on the same space-time domain (1993–2004 period between both polar circles). The 5-member (observations plus 4 simulations) collocated SLA database is then obtained in three further steps: (i) by masking simulated and observed SLAs where and when either real or simulated sea-ice was present, (ii) by removing from each dataset its

1993–1999 temporal average at each grid point (as done routinely in AVISO); and (iii) by removing from each dataset its global average every week.

A one-dimensional low-pass Lanczos filter is then applied twice to split this “raw” collocated SLA database (and, further, to evaluate the model skills) within 3 frequency bands, close to those chosen by Berloff and McWilliams (1999) to analyze the nonlinear response of idealized models at increasing resolution. The first low-pass filtering is applied on raw collocated timeseries with a 18-month cutoff period, and yields the collocated interannual fluctuations of simulated and observed SLAs. The second pass is performed with a 5-month cutoff period to split the remaining signals into “quasi-annual” and “mesoscale” bands. The timescales  $T$  of the interannual, quasi-annual, and mesoscale bands thus correspond to  $T > 18$  months, 5 months  $< T < 18$  months, and 14 days  $< T < 5$  months, respectively.

This paper puts some emphasis on simulated interannual variabilities; the statistics described below are computed in this frequency band from collocated SLA timeseries both (i) directly, and (ii) after an additional low-pass Lanczos isotropic 2-D filtering in space of each collocated SLA map. Comparisons between observed and simulated SLA transects showed that our coarsest-resolution model ( $2^\circ$ ) isotropically resolves spatial scales larger than about  $6^\circ \times \cos(\text{latitude})$ . This cutoff wavelength was thus chosen to further compare observed and simulated interannual SLA characteristics onto the same range of resolved spatial scales, i.e.  $6^\circ$ -to-global; this spatially and temporally low-passed filtered dataset will be denoted as “large-scale interannual”, and will be analyzed in Sect. 7. The 1-D and 2-D filtering techniques are described in Duchon (1979). Figure 2 summarizes the space-time scales considered in the following.

## 2.2.2 Model-observation comparison statistics

Collocated SLA timeseries at location  $(i, j)$  are noted  $\eta^A(i, j, t)$  and  $\eta^m(i, j, t)$  for AVISO observations and for the  $m^{\text{th}}$  model, respectively ( $i \in [1; 1080]$ ,  $j \in [1; 915]$ ,  $t \in [1; 625]$ ,  $m \in [1; 4]$ ). Let  $\bar{\phi}^t$  denote the time average of variable  $\phi$  between 1993 and 2004. At

### Sea-surface variability sensitivity to resolution

T. Penduff et al.

Title Page

Abstract

Introduction

Conclusions

References

Tables

Figures

◀

▶

◀

▶

Back

Close

Full Screen / Esc

Printer-friendly Version

Interactive Discussion



each  $(i, j)$ , we define for  $A$  and for each model  $m$  the temporal standard deviations:

$$\sigma^A(i, j) = \sqrt{\overline{[\eta^A(t) - \overline{\eta^A}^t]^2}} \quad (1)$$

$$\sigma^m(i, j) = \sqrt{\overline{[\eta^m(t) - \overline{\eta^m}^t]^2}}. \quad (2)$$

The ratio  $\sigma^m/\sigma^A$  will be called resolved variability. Temporal model-observation correlation is computed as

$$C_t^m(i, j) = \frac{\overline{(\eta^m(t) - \overline{\eta^m}^t)(\eta^A(t) - \overline{\eta^A}^t)}}{\sigma^m(i, j)\sigma^A(i, j)}. \quad (3)$$

The latitude-dependant agreement between (stationary) maps of  $\sigma^m(i, j)$  and  $\sigma^A(i, j)$  is then quantified in each frequency band as follows: both latter fields are split into 28 zonally-periodic stripes spanning the  $[70^\circ \text{S} - 70^\circ \text{N}]$  latitude range by  $5^\circ$  intervals. Each stripe  $\lambda$  is then reorganized as a long two-dimensional vector of length  $l$  containing elements noted  $\sigma^m(\lambda, l)$  and  $\sigma^A(\lambda, l)$ . Let  $\alpha^A(\lambda)$  and  $\alpha^m(\lambda)$  denote the spatial standard deviations of both latter fields in stripe  $\lambda$ . The spatial correlation coefficient  $C_s^m(\lambda)$  between  $\sigma^m(\lambda, l)$  and  $\sigma^A(\lambda, l)$  is finally computed in the  $\lambda^{th}$  stripe for the  $m^{th}$  model and for each frequency range as:

$$C_s^m(\lambda) = \frac{\overline{(\sigma^m(l) - \overline{\sigma^m}^\lambda)(\sigma^A(l) - \overline{\sigma^A}^\lambda)}}{\alpha^m(\lambda)\alpha^A(\lambda)}, \quad (4)$$

where  $\overline{\phi}^\lambda$  denotes the spatial average of variable  $\phi$  over the  $\lambda^{th}$  latitudinal band. Spatial correlation coefficients between two satellite-derived  $\sigma^A$  fields in distinct frequency ranges will be noted  $C_s^A$ . Note that global spatial correlation coefficients between global  $\sigma(i, j)$  maps are also provided in the following; they simply correspond to  $C_s^m$  or  $C_s^A$  computed over a wide latitudinal band extending between  $66^\circ \text{S}$  and  $66^\circ \text{N}$ .

Title Page

Abstract

Introduction

Conclusions

References

Tables

Figures

◀

▶

◀

▶

Back

Close

Full Screen / Esc

Printer-friendly Version

Interactive Discussion



## Sea-surface variability sensitivity to resolution

T. Penduff et al.

Title Page

Abstract

Introduction

Conclusions

References

Tables

Figures

◀

▶

◀

▶

Back

Close

Full Screen / Esc

Printer-friendly Version

Interactive Discussion



$\sigma^A(i, j)$  and  $\sigma^m(i, j)$  maps are displayed in Fig. 3. In each frequency band, these five  $\sigma(i, j)$  fields and the four  $C_t^m(i, j)$  fields have also been averaged within each of the 28 stripes introduced above to yield  $\sigma^A(\lambda)$ ,  $\sigma^m(\lambda)$ , and  $C_t^m(\lambda)$ , respectively (left and middle column in Fig. 4). The right column in Fig. 4 shows the meridional profiles of  $C_s^m(\lambda)$ , thus complementing the statistical intercomparison synthesis between simulated and observed SLAs as a function of latitude.

In the four following sections, the observed and simulated 1993-2004 SLA standard deviations are compared (without spatial filtering) within the three frequency ranges defined above in terms of intensity, spatial distribution, and temporal phase. The large-scale interannual variability is presented in Sect. 7. We remind the reader that all statistics are based on SLA maps collocated at the same spatio-temporal resolution ( $\frac{1}{3}^\circ \times \frac{1}{3}^\circ \times 7$  days), and that the model resolutions become similar (resp. remain unchanged) in the meridional (resp. zonal) direction toward the equator as shown in Fig. 1.

### 3 Impact of resolution on high frequency (mesoscale) variability

In the real ocean, mesoscale SLA standard deviations reach their maxima (above  $13 \text{ cm} \cdot \text{s}^{-1}$ , see the upper left panel in Fig. 3) in the main eddy-active regions: Gulf Stream (GS)-North Atlantic Current (NAC) and Kuroshio (KS) extensions, Confluence and Agulhas regions, East Australian Current, Mozambique Channel, south of Africa, Australia and America. The mesoscale variability thus approaches  $5 \text{ cm} \cdot \text{s}^{-1}$  on zonal average between  $35\text{--}40^\circ \text{ N}$ ,  $40^\circ \text{ S}$  and  $55\text{--}60^\circ \text{ S}$  (upper left panel in Fig. 4). Secondary maxima, exceeding  $7 \text{ cm} \cdot \text{s}^{-1}$  locally, are found all along the Antarctic Circumpolar Current (ACC), within the Indo-Pacific subtropics ( $20\text{--}30^\circ \text{ S}$  and  $20\text{--}30^\circ \text{ N}$ ), and along the equatorial path of Tropical Instability Waves. Over most of the mid-and high-latitude eastern basins, the background level of observed mesoscale variability lies in the  $3\text{--}6 \text{ cm} \cdot \text{s}^{-1}$  range.

Previous studies showed that compared to other models at similar resolution, the

present  $\frac{1}{4}^\circ$  model simulates well the paths of most main currents, the distribution of the eddy activity (Barnier et al., 2009), and the interactions between topography, the mean and eddy flows (Penduff et al., 2007; Le Sommer et al., 2009). As in many eddy-admitting models, however, certain currents are mislocated at  $\frac{1}{4}^\circ$ : the GS is (moderately) displaced to the North, the NAC tends to follow the Mid-Atlantic Ridge between 44 and 52° N, and the Kuroshio does not extend far enough to the east. The papers cited above provide a detailed assessment of the mean and eddy flows simulated by the  $\frac{1}{4}^\circ$  model.

More quantitatively, spatial correlations  $C_s^m$  between observed and  $\frac{1}{4}^\circ$  mesoscale variability maps lie between 0.6 and 0.8 mostly everywhere (upper right panel in Fig. 4). As expected, spatial correlations strongly decrease with decreasing resolution, which strongly damps and distorts mesoscale variability. There are a few exceptions, though. First, the  $1^\circ$  model has a finer meridional resolution than the  $\frac{1}{2}^\circ$  model around the equator (see Fig. 1), but yields significantly smaller mesoscale spatial correlations in the  $0^\circ$ – $10^\circ$  N band. It is likely that the GM90 parameterization used in the  $1^\circ$  model damps the Tropical Instability Waves that dominate this region in this frequency band (Pezzi et al., 2006). Second, two topographically-confined mesoscale variability peaks can be seen in semi-enclosed basins (Gulf of Carpentaria North of Australia around  $10^\circ$  S, southern Baltic Sea at  $58^\circ$  N, see Fig. 3) in the AVISO and simulated datasets (except at  $2^\circ$ ); their prominence at identical locations within their latitude bands explains the large  $C_s^m$  values found there and the weak impact of resolution on  $C_s^m$  (Fig. 4). Away from these locations, both laminar models yield similar mesoscale  $C_s^m$  values that are smaller than their eddy-admitting counterpart throughout most of the global ocean; regarding this skill measure, the  $\frac{1}{4}^\circ$  model performs better than the  $\frac{1}{2}^\circ$  model almost everywhere, and much better than laminar models.

As expected, mesoscale variability is very weak in both laminar models, i.e. from around 20% of observed levels in the tropics up to 45% near  $60^\circ$  S (Figs. 3 and 4); their meridional distributions are also very similar. Increasing resolution (and decreasing dissipation) yields a monotonic increase in mesoscale variability: 29, 35, 42 and

**Sea-surface  
variability sensitivity  
to resolution**

T. Penduff et al.

Title Page

Abstract

Introduction

Conclusions

References

Tables

Figures

◀

▶

◀

▶

Back

Close

Full Screen / Esc

Printer-friendly Version

Interactive Discussion



**Sea-surface  
variability sensitivity  
to resolution**

T. Penduff et al.

[Title Page](#)[Abstract](#)[Introduction](#)[Conclusions](#)[References](#)[Tables](#)[Figures](#)[◀](#)[▶](#)[◀](#)[▶](#)[Back](#)[Close](#)[Full Screen / Esc](#)[Printer-friendly Version](#)[Interactive Discussion](#)

56% of its globally-averaged observed magnitude are simulated at  $2^\circ$ ,  $1^\circ$ ,  $\frac{1}{2}^\circ$  and  $\frac{1}{4}^\circ$  models, respectively. The  $\frac{1}{4}^\circ$  mesoscale variability roughly accounts for about 50% of its observed levels within  $40^\circ\text{S}$ – $40^\circ\text{N}$ , but both this fraction, and its increase with resolution, are stronger poleward of about  $30^\circ$  (ACC, Agulhas, Confluence areas, sub-polar North Atlantic). It is unlikely that this resolution-induced increase in the portion of SLA variability reproduced at high latitudes comes from a better representation of energetic baroclinic features (i.e. mesoscale eddies). Indeed, these eddy scales follow the internal Rossby radii that decrease polewards much faster than the  $\frac{1}{4}^\circ$  local resolution (Fig. 1). Increasing latitude, however, tends to enhance the contribution of barotropic, topographically-influenced fluctuations on SLA at these frequencies (Guinehut et al., 2006; Vinogradova et al., 2007). This resolution-induced increase in simulated mesoscale SLA variability at high latitudes might thus come from stronger (and/or less damped) barotropic motions.

The upper middle panel in Fig. 4 shows the zonally-averaged correlation coefficients  $C_t^m$  between observed and simulated local SLA timeseries at mesoscale frequencies. The  $2^\circ$  resolution yields the smallest mesoscale temporal correlations in the Northern Hemisphere. In the  $53$ – $60^\circ\text{N}$  band, the  $2^\circ$ -model correlation map (not shown) exhibits indeed a large-scale spatially-coherent drop of these correlation coefficients (about  $-0.1$ ) all along the edges of both the Atlantic and Pacific subpolar gyres. This feature is found at global scale: except in the  $2^\circ$  model, temporal correlations at mesoscale frequencies increase by about  $0.05$  towards the continents over a  $O(1.5^\circ)$  length scale (Fig. 5).

In the Southern Ocean, mesoscale temporal correlations are smallest in the  $\frac{1}{4}^\circ$  simulation. This is consistent with the presence of a strong, chaotic eddy activity along the ACC. Away from the  $5^\circ\text{S}$ – $5^\circ\text{N}$  band where the large correlation ( $0.5$ ) may be attributed to relatively linear dynamics and accurate atmospheric forcings,  $C_t^m$  values reach a mid-latitude minimum. These mid-latitude values remain similar at  $1^\circ$ ,  $\frac{1}{2}^\circ$ , and  $\frac{1}{4}^\circ$  resolutions, despite the monotonic increase with resolution in the intensity of mesoscale variability. The insensitivity of mesoscale temporal correlations to enhanced nonlinear-

ities at mid latitudes contrasts with the Southern ocean, and remains to be explained.

#### 4 Impact of resolution on medium frequency (quasi-annual) variability

The spatial correlation between the global variability maps at quasi-annual and mesoscale bands is large both in the AVISO dataset (0.76), and in the  $\frac{1}{4}^\circ$  model simulation (0.72). Accordingly, the RMS difference between global, observed  $\sigma^A$  maps of quasi-annual and mesoscale variability is relatively small (2.3 cm), and is the same in the  $\frac{1}{4}^\circ$  dataset. In other words, and as can be seen in Fig. 3, most quasi-annual and mesoscale variability maxima are found in the same areas (KS, GS-NAC, Agulhas, ACC, Confluence), both in the AVISO and  $\frac{1}{4}^\circ$  datasets.

Figure 4 shows that the agreement between the observed and  $\frac{1}{4}^\circ$  maps of quasi-annual variability is maximum between  $20^\circ$  S and  $20^\circ$  N ( $C_s^{1/4^\circ} \sim 0.9$ ) and remains good in most regions ( $C_s^{1/4^\circ} \sim 0.6 - 0.7$ ). Decreasing resolution yields a monotonic decrease in  $C_s^m$  values in most regions, especially poleward of  $\pm 20^\circ$ . As in the mesoscale range, quasi-annual spatial correlations are weakest in both laminar simulations, and  $\frac{1}{2}^\circ$  results are intermediate between  $C_s^{1/4^\circ}$  and  $C_s^{2^\circ}$ .

The quasi-annual AVISO SLA standard deviation globally exceeds its mesoscale counterpart by about 10% (up to 80% around  $35^\circ$  N, left panel, second row in Fig. 4). Zonally-averaged simulated variability levels nicely follow the observations north of  $35^\circ$  S lying around 60–90% of their observed value, with only a small impact of resolution. Variability maxima, peaking at quasi-annual timescales, are observed along  $10^\circ$  N ( $\sigma^A \sim 6$ cm) and  $10^\circ$  S ( $\sigma^A \sim 4$ cm) in the Indian and Eastern North Pacific basins (Fig. 3). These zonally-extended maxima are present in the four simulations; their magnitude reach about 70 to 85% of observed levels, except in the  $2^\circ$  model were it drops by another 10%. South of about  $45^\circ$  S, the quasi-annual variability levels remain above 80% of its observed level in the  $\frac{1}{4}^\circ$  simulation, but fall around 50% at  $\frac{1}{2}^\circ$  resolution and below 40% in both laminar runs.

### Sea-surface variability sensitivity to resolution

T. Penduff et al.

Title Page

Abstract

Introduction

Conclusions

References

Tables

Figures



Back

Close

Full Screen / Esc

Printer-friendly Version

Interactive Discussion



## Sea-surface variability sensitivity to resolution

T. Penduff et al.

Title Page

Abstract

Introduction

Conclusions

References

Tables

Figures

◀

▶

◀

▶

Back

Close

Full Screen / Esc

Printer-friendly Version

Interactive Discussion



In all simulations, quasi-annual temporal correlations  $C_t^m$  (Fig. 4) exhibit a marked low-latitude maximum, superimposed on a general decrease between 0.8 around  $60^\circ$  N and 0.3 around  $60^\circ$  S. Whether this north-south contrast is due to less realistic forcing in the Southern Ocean or due to another cause is still unclear. The impact of resolution on quasi-annual  $C_t^m$  values is similar to that found at mesoscale: both eddy-admitting simulations yield  $O(0.05)$  smaller  $C_t^m$  values south of about  $30^\circ$  S, while the coarsest ( $2^\circ$ ) model does not yield the landward increase in temporal correlations found on finer grids (Fig. 5). Atmospherically-forced coastally-trapped processes (upwellings, waves, etc) substantially contribute to the mesoscale and quasi-annual variability in these areas. Our results show that their structure and phase require a  $1^\circ$  or finer resolution to be correctly simulated (provided that AVISO data are accurate enough near the coast). Whether model resolutions finer than  $\frac{1}{4}^\circ$  would further increase (through a more accurate representation of forced signals) or decrease (by admitting more chaotic small-scale turbulence) near-coastal  $C_t^m$  values remains to be determined.

### 5 Impact of resolution on low frequency (interannual) variability

The global spatial correlation coefficient between the interannual and quasi-annual  $\sigma^A$  observed variability maps (the upper two center panels in Fig. 3) is significant (0.72), and about as large as its counterpart between quasi-annual and mesoscale maps (0.76, see previous section). Note that this correspondance between  $\sigma$  maps in the 3 frequency ranges also holds in the  $\frac{1}{4}^\circ$  simulation dataset (second row in Fig. 3): in this latter simulation, the spatial correlation coefficient is 0.70 (resp. 0.72) between quasi-annual and interannual (resp. mesoscale)  $\sigma^{1/4^\circ}$  maps. In other words, both interannual and quasi-annual SLA variabilities happen to be strong in the main eddy-active regions (KS, GS-NAC, Agulhas, ACC, Confluence), in the real ocean and in the  $\frac{1}{4}^\circ$  simulation. This geographical correspondance, which is somewhat less marked at low latitudes, strongly suggests that the interannual variability in several mid- and high-latitude areas is directly influenced by the local mesoscale activity. This hypothesis is

further discussed below.

Interannual timescales are those at which the  $\frac{1}{4}^\circ$  resolution yields the most realistic sea-surface variability intensities: resolved interannual variability reaches 81% globally and at most latitudes. This global fraction reduces to 71% at  $\frac{1}{2}^\circ$  and to 60% in both laminar models. A similar decrease with resolution is seen at quasi-annual timescales (76, 68, 62, 61%, respectively, from  $\frac{1}{4}^\circ$  to  $2^\circ$ ).

The distribution and temporal evolution of simulated interannual variabilities are particularly realistic between  $20^\circ$  S and  $20^\circ$  N (i.e.  $C_s^m$  and  $C_t^m$  values around 0.9 and 0.8, respectively). Moreover both metrics, and the magnitude of the SLA variability, are almost identical in the four simulations in this latitude-frequency band. These results show that the interannual tropical SLA variability is well simulated when the meridional resolution remains in the 30–60 km range, and remains insensitive to both a 8-fold change in zonal resolution and to the choice of parameterizing baroclinic instability through GM90 instead of resolving it.

Poleward of  $\pm 30^\circ$ , the impact of resolution on the intensity, temporal phase, and spatial distribution of simulated interannual variabilities is much more pronounced, and shares interesting similarities with that described at shorter timescales. The third row in Fig. 4 shows that in the interannual band as well, increasing resolution induces (i) a strong, monotonic increase in  $\sigma^m$  (variability intensity, lower left panel), (ii) a strong, monotonic increase in  $C_s^m$  (spatial correlations, lower right panel), and (iii) a weak, monotonic decrease in  $C_t^m$  (temporal correlations, lower middle panel).

These concomitant features quantify the monotonic and beneficial impact of resolution on the distribution and intensity of mid- and high-latitude SLA variability in the mesoscale, quasi-annual, and interannual bands. This improvement goes along with a moderate but systematic decorrelation between the simulated and observed local SLA timeseries, in the three frequency bands. This apparent connection between the impacts of resolution on SLA variability levels, and their spatial and temporal correlations with the observed ocean is investigated in the next section.

**Sea-surface  
variability sensitivity  
to resolution**

T. Penduff et al.

Title Page

Abstract

Introduction

Conclusions

References

Tables

Figures

◀

▶

◀

▶

Back

Close

Full Screen / Esc

Printer-friendly Version

Interactive Discussion



## 6 Link between resolution-induced changes in variability levels and correlations

We have shown that increasing resolution may substantially change the intensity, distribution, and temporal phase of SLA variability, depending on regions of the World Ocean and the frequency band. In this section we attempt to relate these changes together and to quantify these links.

The magenta circles in the upper left panel in Fig. 6a show for the mesoscale frequency band how the transition from  $2^\circ$  to  $1^\circ$  resolution simultaneously increases, within each latitudinal band (each circle), both zonally-averaged resolved SLA variability levels (i.e.  $(\sigma^{1^\circ} - \sigma^{2^\circ})/\sigma^A > 0$ , abscissae) and zonally-averaged temporal correlations ( $C_t^{1^\circ} - C_t^{2^\circ} > 0$ ). Robust regression on these dots (line, and Fig. 6b) indicates that at all latitudes for this resolution transition, a 10% increase in mesoscale  $\sigma^m/\sigma^A$  is significantly associated with a local 0.04 increase in  $C_t^m$ . Mismatches between observed and simulated SLA timeseries are thus reduced when resolution goes from  $2^\circ$  to  $1^\circ$  in the mesoscale (and to a lesser extent the quasi-annual) frequency range.

This latter feature is an exception, though. Figures 6a, b show that in all other cases, resolution-induced increases in SLA variability levels yield decorrelations in time between simulated and observed timeseries within the same latitude band. This general result persists when the 3 resolution changes are regressed together (dashed lines in Fig. 6-a's left panels, uppermost squares in Fig. 6b's left panel): everywhere increased model resolution enhances the resolved variability by 10%, one may expect a 0.01–0.04 decrease in temporal correlations. This link is robust, but the regression slope is weak, though: Fig. 4 shows that the typical 30–40%  $\sigma$  increases with resolution yield only small temporal decorrelations. The Southern Ocean is the only region where at all timescales, resolution increases SLA variability levels enough to yield substantial decorrelations in time.

The right panels in Figs. 6a, b confirms another robust impact of resolution and subsequent increases in SLA variability levels. Besides the  $2^\circ$  to  $1^\circ$  transition in which

Title Page

Abstract

Introduction

Conclusions

References

Tables

Figures



Back

Close

Full Screen / Esc

Printer-friendly Version

Interactive Discussion



## Sea-surface variability sensitivity to resolution

T. Penduff et al.

Title Page

Abstract

Introduction

Conclusions

References

Tables

Figures

◀

▶

◀

▶

Back

Close

Full Screen / Esc

Printer-friendly Version

Interactive Discussion



interannual variability gets stronger but yields smaller spatial correlation ( $C_s^m$ ) values, higher resolution yields at all frequencies both a stronger SLA variability and local improvements of its geographical distribution. The large regression slopes found between  $\Delta\sigma^m/\sigma^A$  and  $C_s^m$  (+10% in resolved variability yields about +0.1 in spatial correlation) confirm that in all frequency ranges, SLA variability maps rapidly converge towards their observed counterparts when resolution (i.e. where variability levels) increase. This link is clearest at mesoscale frequencies, but remains robust at quasi-annual and interannual timescales from  $1^\circ$  to  $\frac{1}{4}^\circ$ .

### 7 On the large-scale interannual variability

The comparison of observed and simulated interannual variabilities is now restricted to spatial scales larger than  $6^\circ$ . This focuses the analysis on the patterns that are actually resolved in all 5 datasets, including the  $2^\circ$  simulation, and by laminar oceans used in most present coupled models. We also assess in this way how the explicit resolution of scales smaller than  $6^\circ$  can affect the simulation of scales larger than this threshold. Note that the spatial filtering of interannual variabilities is not performed on  $\sigma$  maps but on individual weekly SLA collocated maps. The right column in Fig. 3 and last row in Fig. 4 show the distributions of SLA standard deviations, temporal and spatial correlations in this large-scale interannual band.

In both the observed and  $\frac{1}{4}^\circ$  datasets, the spatially-filtered interannual variability is about 50% weaker than its unfiltered counterpart in the GS, and in the ACC between 20 and  $75^\circ$  E (compare the uppermost two panels in the last two columns in Fig. 3): half of the interannual standard deviation of SLA there is thus accounted for by spatial scales smaller than  $6^\circ$ . Along with the alignment of mesoscale, quasi-annual, and interannual variabilities mentioned before on unsmoothed SLA variabilities, this latter feature strongly suggests that in those two regions, relatively small-scale features (probably mesoscale eddies produced by these unstable currents) locally generate strong SLA fluctuations over the full range of timescales resolved in the present dataset. A

decrease in interannual variability levels after spatial filtering (and therefore a small-scale confinement of broad-band temporal variability emission) is also noticeable in the AVISO and  $\frac{1}{4}^\circ$  datasets in the Confluence region (and the Pacific sector of the ACC to a lesser extent). This observed feature is absent at coarser resolutions where the broad-band temporal variability of SLA (from weeks to years) is largely accounted for by large-scale motions instead of mesoscale eddies. This explains the strong improvement seen at  $\frac{1}{4}^\circ$  in SLA variability levels in these two eddying regions, especially in the Southern Ocean (first column in Fig. 4). Scales smaller than  $6^\circ$ , which are partially resolved at  $\frac{1}{4}^\circ$ , increase by about 16% the Southern Ocean interannual variability in zonal average between  $40^\circ$  and  $60^\circ$  S (compare the black lines, lowestmost two panels, left column in Fig. 4); this agrees well with the observations (green lines) where this percentage is about 13.8%. Away from eddy-active regions, in particular the Southern Ocean and the GS area, the last two columns in Fig. 3 are much more similar in both the observations and the four simulations, suggesting that the interannual variability is mostly accounted for by motions with scales larger than  $6^\circ$ . Note that the spatial coincidence between regions of resolution-induced enhanced variability and modified correlations (discussed in Sect. 6 in the unsmoothed case) is less clear (statistically insignificant) in the large-scale interannual band.

More generally, the last two rows in Fig. 4 show that the impacts of resolution increases that were highlighted earlier in the absence of spatial filtering (i.e. monotonic increase in interannual variabilities, slight decorrelation in SLA timeseries, marked improvement of the maps of interannual variability patterns) are essentially the same when motions with scales smaller than  $6^\circ$  are omitted. Note that choosing a  $12^\circ$  cutoff lengthscale instead of  $6^\circ$  yields the same general results, with moderate quantitative changes: in this very large-scale interannual band, increased resolution from  $2^\circ$  to  $\frac{1}{4}^\circ$  enhances the standard deviation of SLA fluctuations (+15–20% poleward of  $40^\circ$ ), decreases temporal correlations by up to 0.2 south of  $40^\circ$  S, and enhances spatial correlations by about 0.2 poleward of  $30^\circ$ .

---

**Sea-surface  
variability sensitivity  
to resolution**T. Penduff et al.

---

[Title Page](#)[Abstract](#)[Introduction](#)[Conclusions](#)[References](#)[Tables](#)[Figures](#)[⏪](#)[⏩](#)[◀](#)[▶](#)[Back](#)[Close](#)[Full Screen / Esc](#)[Printer-friendly Version](#)[Interactive Discussion](#)

## 8 Conclusions

The aim of this study was to quantitatively assess the realism of the sea-surface variability simulated between 1993 and 2004 in four global ocean/sea-ice 50-year simulations performed with identical surface forcing by the DRAKKAR Group at increasing horizontal resolutions ( $2^\circ$ ,  $1^\circ$ ,  $\frac{1}{2}^\circ$ , and  $\frac{1}{4}^\circ$ ). Outputs from the four simulations have been collocated in time and space onto observed (AVISO) sea level anomaly (SLA) maps, thus yielding a consistent 5-member (SLA) dataset, which was then filtered in time and space. Model-observation comparisons have been performed within three frequency ranges (interannual, quasi-annual, mesoscale), in terms of geographical distribution of sea-level variability, intensity of SLA standard deviations, and correlations between observed and simulated local SLA timeseries. This comparison thus provides a quantitative benchmark regarding the comparative skills of two climate-oriented, laminar models ( $2^\circ$  and  $1^\circ$ ) and two eddy-admitting models ( $\frac{1}{2}^\circ$  and  $\frac{1}{4}^\circ$ ) at various frequencies. The main results are summarized below:

- In all regions, increasing resolution from  $2^\circ$  to  $\frac{1}{4}^\circ$  monotonically enhances mesoscale SLA standard deviations (from 29 to 56% of observed levels in global average). This modest performance at  $\frac{1}{4}^\circ$  is explained in part by the still moderate resolution, but might also be due to the absence of small spatial scales in the atmospheric forcing (Milliff et al., 1996); this leaves room for improvement through further resolution increases and more realistic forcing.
- SLA standard deviations significantly increase with resolution in the quasi-annual and interannual ranges as well (i.e. from 61 to 76% and from 59 to 81% of globally-averaged observed levels, respectively).
- A robust regression analysis showed that throughout the Global Ocean, and within the three frequencies bands, these resolution-induced increases in SLA variability levels are associated over the same latitude bands with (i) large improvements in simulated variability maps, and (ii) slight deteriorations of correlation coefficients

### Sea-surface variability sensitivity to resolution

T. Penduff et al.

Title Page

Abstract

Introduction

Conclusions

References

Tables

Figures



Back

Close

Full Screen / Esc

Printer-friendly Version

Interactive Discussion



## Sea-surface variability sensitivity to resolution

T. Penduff et al.

Title Page

Abstract

Introduction

Conclusions

References

Tables

Figures

◀

▶

◀

▶

Back

Close

Full Screen / Esc

Printer-friendly Version

Interactive Discussion



between simulated and observed timeseries. The skills of the  $2^\circ$  and  $1^\circ$  models are very similar with respect to our three criteria.

- Quasi-annual and mesoscale temporal correlations are slightly (0.05) weaker in the  $2^\circ$  simulation over a  $1.5^\circ$ -wide band along the continents. The spatial scales of seasonal upwellings and of Kelvin waves (whose timescales match these two bands, respectively), and thus the forced response and adjustment of coastal and shelf areas to the atmosphere or to remote oceanic regions, are certainly not well resolved at  $2^\circ$ . Resolutions much finer than  $\frac{1}{4}^\circ$  are needed to properly resolve near-coastal dynamics and forcings (Capet et al., 2004), but it is plausible that enhanced nonlinearities that would emerge on much finer grids would tend to bring temporal correlations to lower levels.
- North of about  $30^\circ$  S, resolution-induced increases in SLA variability levels and associated improvement in their spatial distributions are substantial, but barely modify ( $\pm 5\%$ ) the temporal correlation coefficients between observed and simulated local SLA timeseries.
- The three consequences of resolution increases are maximum in the Southern Ocean: +100% increase of SLA variability levels from  $2^\circ$  to  $\frac{1}{4}^\circ$  in the three frequency bands; strong improvement of SLA variability distributions; 0.1–0.2 decreases in temporal correlations. In regions of strong eddying activity, thus over a significant part of the Southern Ocean, strong quasi-annual and interannual variabilities are found where mesoscale variability is strong as well. The resolution-induced decrease in temporal correlations does thus not necessarily indicate a deterioration of the model skills: it is likely due to the emergence of an eddy-driven broad-band variability, which is partly resolved at  $\frac{1}{4}^\circ$  resolution.
- With respect to  $\sigma^m(\lambda)$  and  $C_s^m(\lambda)$  values, the realism of the  $\frac{1}{2}^\circ$  solution at most frequencies and latitudes is intermediate between its  $2^\circ$  (least realistic) and  $\frac{1}{4}^\circ$  (most realistic) counterparts. The  $1^\circ$  resolution yields a noticeable improvement

**Sea-surface  
variability sensitivity  
to resolution**

T. Penduff et al.

Title Page

Abstract

Introduction

Conclusions

References

Tables

Figures

◀

▶

◀

▶

Back

Close

Full Screen / Esc

Printer-friendly Version

Interactive Discussion



in quasi-annual tropical  $C_s^m$  values compared to the  $2^\circ$  resolution. Besides this exception, both laminar models yield strikingly similar results in most latitude-frequency bands (Fig. 4), despite a twofold resolution ratio. This similarity is maybe due to the use in the  $2^\circ$  and  $1^\circ$  models of the GM90 parametrization, which might have a similar damping and distorting influence on tropical instability waves, quasi-annual and mesoscale variabilities worldwide, and the interannual variability south of  $30^\circ$  S. Assessing this hypothesis would require e.g. a  $\frac{1}{2}^\circ$  simulation with GM90; this is left for future studies.

- These (beneficial) impacts of increased resolution on the interannual variability persist (despite minor quantitative changes) when spatial scales smaller than  $6^\circ$  (or  $12^\circ$ ) are filtered out of collocated SLA fields. This means that the explicit resolution of small scales substantially improves many aspects of the ocean variability at larger space and time scales, i.e. the scales that are presently resolved in ocean-atmosphere coupled models. This benefit of eddy-admitting resolution had not been quantified previously, and might be important for the design of future climate prediction systems.

These results show that eddy-admitting ocean models yield a large improvement over laminar models in terms of sea-surface variability (levels, locations) over most of the global ocean, throughout the whole range of timescales considered here (15 day–6 year). Enhanced model resolution also improves the simulated interannual variability at space scales much larger than model resolutions, i.e. at scales that are largely involved in ocean-atmosphere coupling ( $6^\circ$  to global). Our conclusions thus support and extend the pioneering work by Roberts et al. (2004) about laminar and eddy-admitting ocean models, which will certainly remain important tools for a long time, at least for paleoclimatic studies, and for IPCC-like ensemble climate predictions, respectively.

*Acknowledgements.* The authors would like to thank Gurvan Madec and the NEMO Team for numerous technical and scientific interactions, and Jean-Michel Brankart for interesting discussions. This work is a contribution of the DRAKKAR project, which is supported by the Centre

National d'Etudes Spatiales (CNES) through the Ocean Surface Topography Science Team (OST/ST), by the Centre National de la Recherche Scientifique (CNRS), the Institut National des Sciences de l'Univers (INSU), the Groupe Mission Mercator Coriolis (GMMC). Computations presented in this study were performed at Institut du Développement et des Ressources en Informatique Scientifique (IDRIS). Partial support from the European Commission under Contract SIP3-CT-2003-502885 (MERSEA project) is gratefully acknowledged.



The publication of this article is financed by CNRS-INSU.

## References

- Arakawa, A. and Lamb, V.: A potential enstrophy and energy conserving scheme for the shallow water equations, *Mon. Weather Rev.*, 109, 18–36, 1981. 1519
- Barnier, B., Madec, G., Penduff, T., Molines, J.-M., Treguier, A.-M., le Sommer, J., Beckmann, A., Biastoch, A., Böning, C., Dengg, J., Derval, C., Durand, E., Gulev, S., Remy, E., Talandier, C., Theetten, S., Maltrud, M., McClean, J., and de Cuevas, B.: Impact of partial steps and momentum advection schemes in a global circulation model at eddy permitting resolution, *Ocean Dynam.*, 59, 537, doi:10.1007/s10236-009-0180-y, 2009. 1518, 1524
- Beckmann, A., Böning, C., Köberle, C., and Willebrand, J.: Effects of increased horizontal resolution in a simulation of the North Atlantic Ocean, *J. Phys. Oceanogr.*, 24, 326–344, 1994. 1517
- Berloff, P. S. and McWilliams, J. C.: Large-Scale, Low-Frequency Variability in Wind-Driven Ocean Gyres, *J. Phys. Oceanogr.*, 29, 1925–1949, 1999. 1521
- Böning, C. and Bryan, F. O.: The Warmwatersphere of the North Atlantic Ocean, chap. Large-scale transport processes in high-resolution circulation models, 91–128, *Gebrüder Borntraeger*, 1996. 1517

OSD

6, 1513–1545, 2009

## Sea-surface variability sensitivity to resolution

T. Penduff et al.

Title Page

Abstract

Introduction

Conclusions

References

Tables

Figures

◀

▶

◀

▶

Back

Close

Full Screen / Esc

Printer-friendly Version

Interactive Discussion



**Sea-surface  
variability sensitivity  
to resolution**

T. Penduff et al.

Title Page

Abstract

Introduction

Conclusions

References

Tables

Figures

◀

▶

◀

▶

Back

Close

Full Screen / Esc

Printer-friendly Version

Interactive Discussion



- Böning, C. and Budich, R. G.: Eddy Dynamics in a Primitive Equation Model: Sensitivity to Horizontal Resolution and Friction, *J. Phys. Oceanogr.*, 22, 361–381, 1992. 1517
- Brodeau, L., Barnier, B., Treguier, A.-M., and Penduff, T.: Comparing sea surface atmospheric variables from ERA40 and CORE with a focus on global net heat flux, 2006. 1518
- 5 Brodeau, L., Barnier, B., Treguier, A.-M., Penduff, T., and Gulev, S.: An ERA40-based atmospheric forcing for global ocean circulation models, *Ocean Model.*, in revision, 2009. 1518
- Capet, X., Marchesiello, P., and McWilliams, J.: Upwelling response to coastal wind profiles, *Geophys. Res. Lett.*, 31, L13311, doi:10.1029/2004GL020123, 2004. 1533
- Chanut, J., Barnier, B., Large, W. G., Debreu, L., Penduff, T., Molines, J.-M., and Mathiot, P.: Mesoscale Eddies in the Labrador Sea and their Contribution to Convection and Restratification, *J. Phys. Oceanogr.*, 38, 1617–1643, doi: 10.1175/2008JPO3485.1, 2008. 1516
- 10 Chelton, D. B., de Szoeke, R. A., Schlax, M. G., Naggar, K. E., and Siwertz, N.: Geographical variability of the first-baroclinic Rossby radius of deformation, *J. Phys. Oceanogr.*, 28, 433–460, 1998. 1540
- 15 Cravatte, S., Madec, G., Izumo, T., Menkes, C., and Bozec, A.: Progress in the 3-D circulation of the eastern equatorial Pacific in a climate ocean model, *Ocean Model.*, 17, 28–48, 2007. 1519, 1520
- Dengg, J., Beckmann, A., and Gerdes, R.: The Gulf Stream separation problem, in: *The Warmwatersphere of the North Atlantic Ocean*, edited by: Krauss, W., 253–290, Gebrüder Borntraeger, Berlin, 1996. 1517
- 20 Drillet, Y., Bourdallé-Badie, R., Siefriidt, L., and Le Provost, C.: Meddies in the Mercator North Atlantic and Mediterranean Sea eddy-resolving model, *J. Geophys. Res.*, 110, C03016, doi: 10.1029/2003JC002170, 2005. 1516
- Duchon, C.: Lanczos Filtering in One and Two Dimensions, *J. Appl. Meteorol.*, 18, 1016–1022, 1979. 1521
- 25 DYNAMO Group: DYNAMO: Dynamics of North Atlantic Models. Simulation and assimilation with high resolution models, Tech. rep., Ber. Inst. f. Meeresk. Kiel, 294, 1997. 1517
- Fanning, A. and Weaver, A.: A horizontal resolution and parameter sensitivity study of heat transport in an idealized coupled climate model, *J. Climate*, 10, 2469–2478, 1997. 1517
- 30 Gent, P. R. and McWilliams, J. C.: Isopycnal Mixing in Ocean Circulation Models, *J. Phys. Oceanogr.*, 20, 150–155, 1990. 1516
- Griffies, S. M., Biastoch, A., Böning, C., Bryan, F. O., Danabasoglu, G., Chassignet, E. P., England, M. H., Gerdes, R., Haak, H., Hallberg, R., Hazeleger, W., Jungclaus, J., Large, W. G.,

---

**Sea-surface  
variability sensitivity  
to resolution**

---

T. Penduff et al.

[Title Page](#)[Abstract](#)[Introduction](#)[Conclusions](#)[References](#)[Tables](#)[Figures](#)[◀](#)[▶](#)[◀](#)[▶](#)[Back](#)[Close](#)[Full Screen / Esc](#)[Printer-friendly Version](#)[Interactive Discussion](#)

Madec, G., Pirani, A., Samuels, B., Scheinert, M., Gupta, A. S., Severijns, C., Simmons, H. L., Treguier, A.-M., Winton, M., Yeager, S., and Yin, J.: Coordinated ocean-ice reference experiments (COREs), *Ocean Model.*, 26, 1–46, 2009. 1519

Guinehut, S., Traon, P.-Y. L., and Larnicol, G.: What can we learn from global altimetry/hydrography comparisons?, *Geophys. Res. Lett.*, 33, L10604, doi:10.1029/2005GL025551, 2006. 1525

Gulev, S. K., Barnier, B., Molines, J.-M., Penduff, T., and Chanut, J.: Impact of spatial resolution on simulated surface water mass transformations in the Atlantic, *Ocean Model.*, 19, 138–160, 2007. 1517

Haidvogel, D. B., Arango, H. G., Hedstrom, K., Beckmann, A., Malanotte-Rizzoli, P., and Shchepetkin, A. F.: Model evaluation experiments in the North Atlantic Basin: simulations in nonlinear terrain-following coordinates, *Dyn. Atmos. Oceans*, 32, 239–281, 2000. 1517

Hecht, M. and Hasumi, H.: Ocean Modeling in an Eddy Regime, 177, AGU Monograph Series, 2008. 1516

Hecht, M. W. and Smith, R. D.: Ocean Modeling in an Eddy Regime, chap. Towards a Physical Understanding of the North Atlantic: A Review of Model Studies in an Eddy Regime, *Geophysical Monograph Series*, American Geophysical Union, 2008. 1516

Holland, W., Harrison, D., and Semtner, A.: Eddies in Marine Science, chap. Eddy-resolving numerical models of large-scale ocean circulation, 379–403, Springer-Verlag, 1983. 1517

Kelly, K. A., Thompson, L., Cheng, W., and Metzger, E. J.: Evaluation of HYCOM in the Kuroshio Extension region using new metrics, *J. Geophys. Res.*, 112, 2007. 1516

Le Sommer, J., Penduff, T., Theetten, S., Madec, G., and Barnier, B.: How momentum advection schemes influence current-topography interactions at eddy-permitting resolution, *Ocean Modelling*, in press, doi:10.1016/j.ocemod.2008.11.007, 2009. 1519, 1524

Levitus, S., Boyer, T., Conkright, M., O'Brian, T., Antonov, J., Stephens, C., Stathopoulos, L., Johnson, D., and Gelfeld, R.: World Ocean Database 1998, Tech. Rep. NESDID18, NOAA Atlas, 1998. 1519

Madec, G.: NEMO reference manual, ocean dynamics component : NEMO-OPA. Preliminary version, Tech. Rep. 27, Note du Pôle de modélisation, Institut Pierre-Simon Laplace (IPSL), France, ISSN No 1288-1619, 2008. 1518

Masumoto, Y., Sasaki, H., Kagimoto, T., Komori, N., Ishida, A., Sasai, Y., Miyama, T., Motoi, T., Mitsudera, H., Takahashi, K., Sakuma, H., and Yamagata, T.: A fifty-year eddy-resolving simulation of the world ocean: Preliminary outcomes of OFES (OGCM for the Earth Simulator),

---

**Sea-surface  
variability sensitivity  
to resolution**


---

T. Penduff et al.

[Title Page](#)
[Abstract](#)
[Introduction](#)
[Conclusions](#)
[References](#)
[Tables](#)
[Figures](#)




[Back](#)
[Close](#)
[Full Screen / Esc](#)
[Printer-friendly Version](#)
[Interactive Discussion](#)


J. Earth Simulator, 1, 35–56, 2004. 1516

Drakkar Group: Eddy-permitting ocean circulation hindcasts of past decades, CLIVAR Exchanges, 12, 8–10, 2007. 1517, 1519

5 McClean, J., Poulain, P.-M., Pelton, J. W., and Maltrud, M.: Eulerian and Lagrangian Statistics from Surface Drifters and a High-Resolution POP Simulation in the North Atlantic, J. Phys. Oceanogr., 32, 2472–2491, 2002. 1516

Milliff, R. F., Large, W. G., Holland, W. R., and McWilliams, J. C.: The general circulation responses of high-resolution North Atlantic Ocean models to synthetic scatterometer winds, J. Phys. Oceanogr., 26, 1747–1768, 1996. 1532

10 Molines, J.-M., Barnier, B., Penduff, T., Brodeau, L., Treguier, A.-M., Theetten, S., and Madec, G.: Definition of the interannual experiment ORCA025-G70, 1958–2004, Tech. Rep. LEGI-DRA-2-11-200, LEGI, available at <http://www.ifremer.fr/lpo/drakkar>, 2006. 1519

Penduff, T., Sommer, J. L., Barnier, B., Treguier, A.-M., Molines, J.-M., and Madec, G.: Influence of numerical schemes on current-topography interactions in  $1/4^\circ$  global ocean simulations, 15 Ocean Sci., 3, 509–524, 2007, <http://www.ocean-sci.net/3/509/2007/>. 1516, 1518, 1519, 1524

Pezzi, L., Caltabiano, A., and Challenor, P.: Satellite observations of the Pacific tropical instability wave characteristics and their interannual variability, Int. J. Remote Sens., 27, 1581–1999, 2006. 1524

20 Roberts, M., Banks, H., Gedney, N., Gregory, J., Hill, R., Mullerworth, S., Pardaens, A., Rickard, G., Thorpe, R., and Wood, R.: Impact of an Eddy-Permitting Ocean Resolution on Control and Climate Change Simulations with a Global Coupled GCM, J. Climate, 17, 3–20, 2004. 1534

Scott, R. B. and Arbic, B. K.: Spectral Energy Fluxes in Geostrophic Turbulence: Implications for Ocean Energetics, J. Phys. Oceanogr., 37, 673–688, 2007. 1516

25 Semtner, A. and Chervin, R.: A simulation of the global ocean circulation with resolved eddies, J. Geophys. Res., 93, 15502–15522, 1988a. 1517

Semtner, A. and Chervin, R.: Ocean general circulation from a global eddy-resolving model, J. Geophys. Res., 97, 5493–5550, 1988b. 1517

30 Smith, R., Maltrud, M., Bryan, F., and Hecht, M.: Numerical simulation of the North Atlantic Ocean at  $1/10^\circ$ , J. Phys. Oceanogr., 30, 1532–1561, 2000. 1516

Street, J. O., Carroll, R. J., and Ruppert, D.: A Note on Computing Robust Regression Estimates Via Iteratively Reweighted Least Squares, The American Statistician, 42, 152–154,

1988. 1545

Timmermann, A., Goosse, H., Madec, G., Fichefet, T., Ethe, C., and Dulière, V.: On the representation of high latitude processes in the ORCA-LIM global coupled sea-ice ocean model, *Ocean Model.*, 8, 175–201, 2005. 1519

5 Treguier, A.-M., Theetten, S., Chassignet, E., Penduff, T., Smith, R., and Talley, L.: The North Atlantic subpolar gyre in four high resolution models, *J. Phys. Oceanogr.*, 35, 757–774, 2005. 1516

10 Treguier, A.-M., England, M. H., Rintoul, S. R., Madec, G., le Sommer, J., and Molines, J.-M.: Southern Ocean overturning across streamlines in an eddy simulation of the Antarctic Circumpolar Current, *Ocean Sci.*, 3, 491–507, 2007, <http://www.ocean-sci.net/3/491/2007/>. 1518, 1519

Vinogradova, N. T., Ponte, R. M., and Stammer, D.: Relation between sea level and bottom pressure and the vertical dependence of oceanic variability, *Geophys. Res. Lett.*, 34, L03608, doi:10.1029/2006GL028588, 2007. 1525

15 Zhai, X., Greatbatch, R. J., and Sheng, J.: Diagnosing the role of eddies in driving the circulation of the northwest Atlantic Ocean, *Geophys. Res. Lett.*, 31, 1–4, 2004. 1516

OSD

6, 1513–1545, 2009

---

**Sea-surface  
variability sensitivity  
to resolution**

T. Penduff et al.

---

Title Page

Abstract

Introduction

Conclusions

References

Tables

Figures

⏪

⏩

◀

▶

Back

Close

Full Screen / Esc

Printer-friendly Version

Interactive Discussion



Sea-surface  
variability sensitivity  
to resolution

T. Penduff et al.

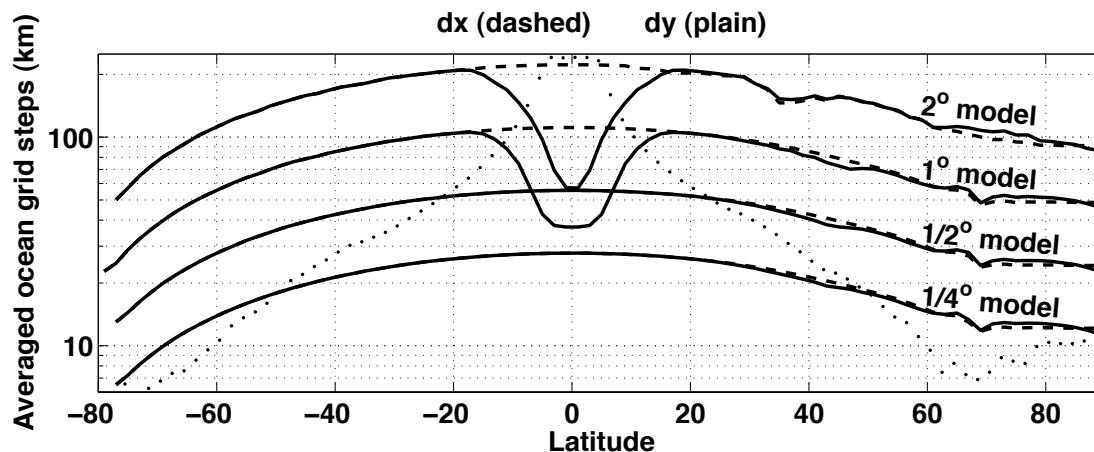


**Fig. 1.** Zonally-averaged zonal (dashed) and meridional (plain) resolution of the four model grids (m, log scale). The meridional resolution increases near the equator in the 2° and 1° models. Dots indicate zonally-averaged first Rossby radii from Chelton et al. (1998).

[Title Page](#)[Abstract](#)[Introduction](#)[Conclusions](#)[References](#)[Tables](#)[Figures](#)[⏪](#)[⏩](#)[◀](#)[▶](#)[Back](#)[Close](#)[Full Screen / Esc](#)[Printer-friendly Version](#)[Interactive Discussion](#)

## Sea-surface variability sensitivity to resolution

T. Penduff et al.

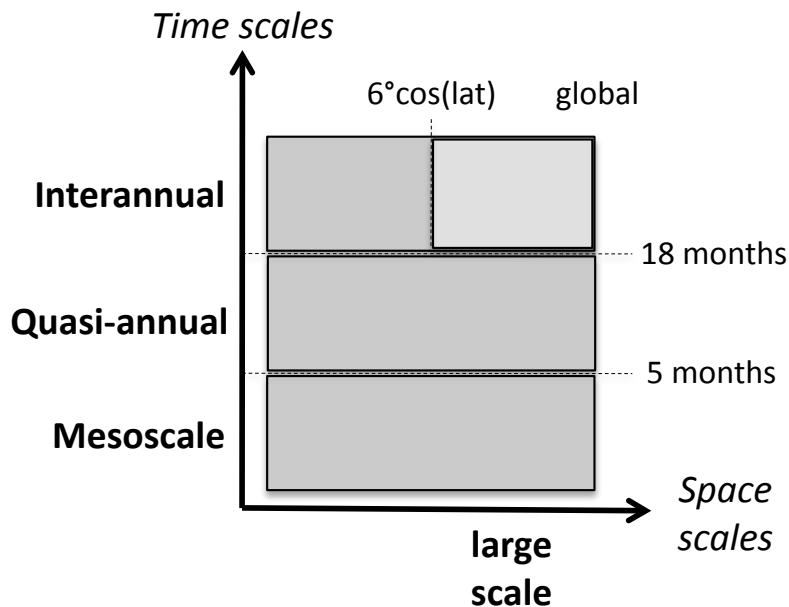


**Fig. 2.** Scheme of the 4 spectral bands in which model-observation comparisons are performed. Mesoscale, Quasi-annual, and Interannual datasets refer to contiguous frequency bands without spatial filtering (medium gray shading). The Large-scale Interannual dataset is shown with a light gray shading.

Title Page

Abstract

Introduction

Conclusions

References

Tables

Figures

◀

▶

◀

▶

Back

Close

Full Screen / Esc

Printer-friendly Version

Interactive Discussion



## Sea-surface variability sensitivity to resolution

T. Penduff et al.

Title Page

Abstract

Introduction

Conclusions

References

Tables

Figures



Back

Close

Full Screen / Esc

Printer-friendly Version

Interactive Discussion

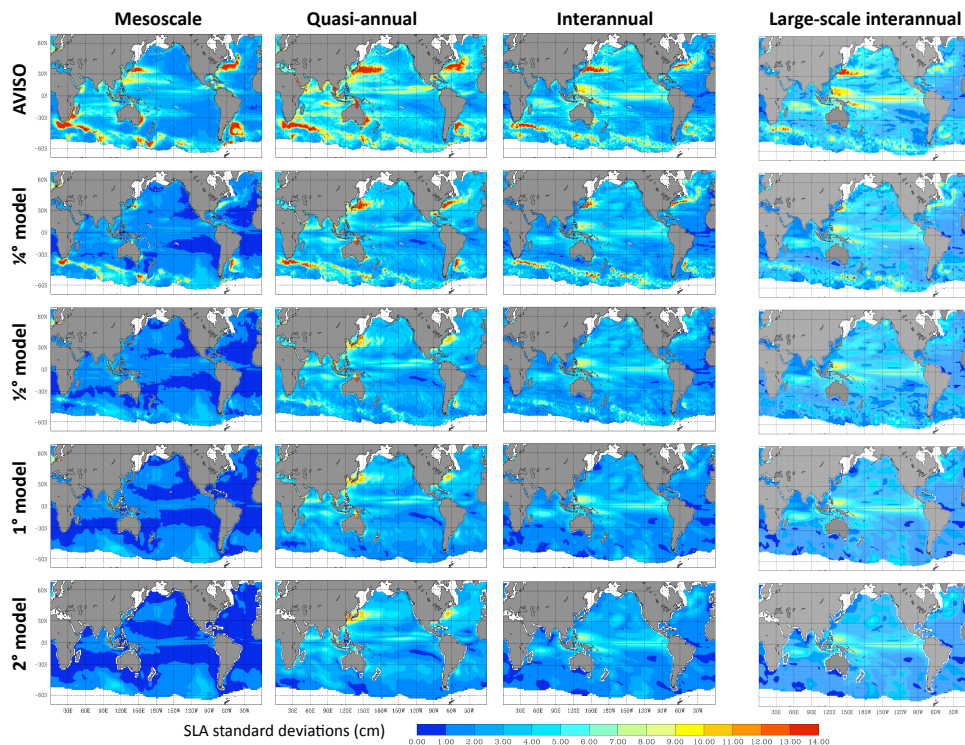


**Fig. 3.** Maps of sea-level variability (standard deviation  $\sigma$  of SLA, cm) computed from the model/observation collocated SLA dataset. Results are shown for the AVISO observations, the  $\frac{1}{4}^\circ$ ,  $\frac{1}{2}^\circ$ ,  $1^\circ$ , and  $2^\circ$  model simulations (from top to bottom). The first three columns derive from SLA fields that were not filtered in space, but filtered in time: mesoscale band (periods shorter than 5 months, first column), the quasi-annual band (periods between 5 and 18 months, second column), and the interannual band (periods longer than 18 months, third column). The fourth column derives from SLA fields that were low-passed filtered both in time and space (periods longer than 18 months and space scales larger than  $6^\circ \times \cos(\text{latitude})$ ).

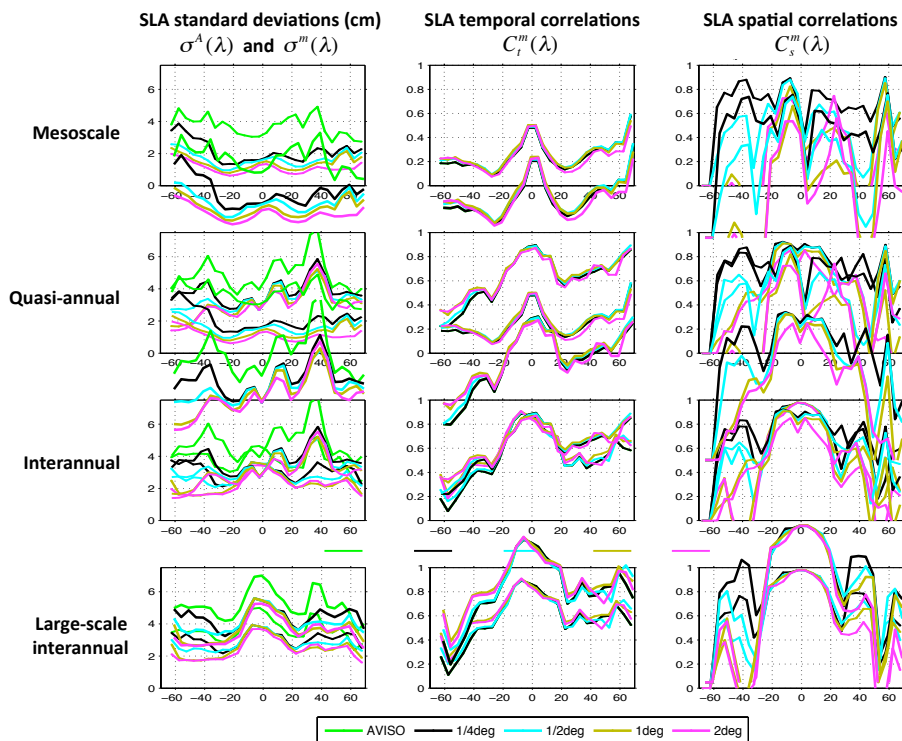


**Fig. 4.** Spatial and temporal statistics of the 5 collocated 1993–2004 SLA datasets in the mesoscale (first row), quasi-annual (second row), interannual (third row), and large-scale interannual (fourth row, see Fig. 3’s legend) bands. Results are computed within  $5^\circ$ -wide latitude bands (abscissae). Left panels: zonal averages of standard deviations of local  $\eta(t)$  timeseries in each dataset ( $\sigma$ , cm). Middle panels: zonal averages of local correlations between observed and each simulated  $\eta(t)$  timeseries. Right panels: zonal averages of spatial correlations between observed and each simulated map of SLA standard deviation.

[Title Page](#)
[Abstract](#)
[Introduction](#)
[Conclusions](#)
[References](#)
[Tables](#)
[Figures](#)
[◀](#)
[▶](#)
[◀](#)
[▶](#)
[Back](#)
[Close](#)
[Full Screen / Esc](#)
[Printer-friendly Version](#)
[Interactive Discussion](#)


Sea-surface  
variability sensitivity  
to resolution

T. Penduff et al.

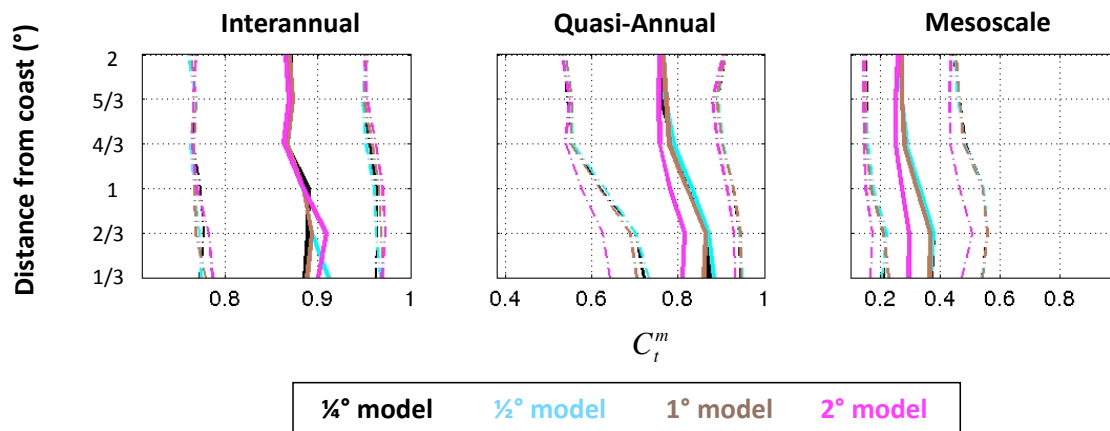


**Fig. 5.** Global evolution of local model-observation temporal correlations  $C_t^m$  (abscissae) at various distances from the coast (ordinates, °), in the interannual (left), quasi-annual (middle) and mesoscale (right) frequency bands. For each frequency band and each simulation, plain lines show the median of all  $C_t^m$  values in the global Ocean located at a given distance. Dashed lines show the 17% and 83% percentiles associated with each distribution.

Title Page

Abstract

Introduction

Conclusions

References

Tables

Figures

◀

▶

◀

▶

Back

Close

Full Screen / Esc

Printer-friendly Version

Interactive Discussion



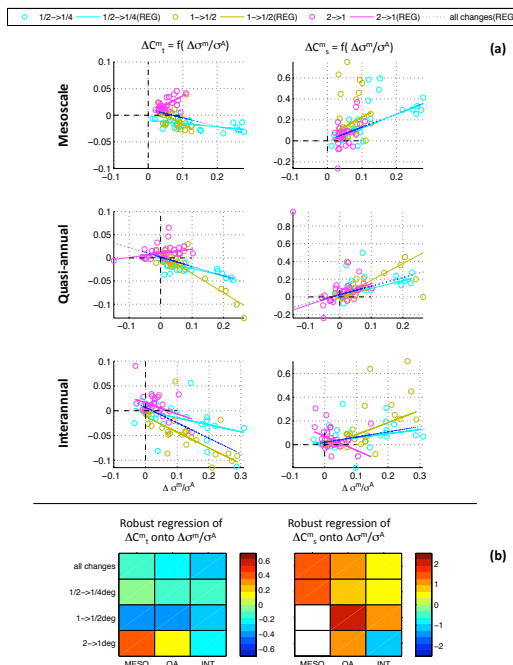


**Fig. 6.** (a) Scatterplots of resolution-induced changes in  $C_t^m$  (temporal correlations, left) and in  $C_s^m$  (spatial correlations, right) as a function of the resolution-induced changes in  $\sigma^m / \sigma^A$  (resolved SLA variabilities in abscissae). Each circle concerns a latitude band  $\lambda$ ; these circles are located at abscissae  $(\sigma^{m+1}(\lambda) - \sigma^m(\lambda)) / \sigma^A(\lambda)$ , and at ordinates  $C_t^{m+1}(\lambda) - C_t^m(\lambda)$  (left) or  $C_s^{m+1}(\lambda) - C_s^m(\lambda)$  (right). The index  $m$  corresponds to model resolutions increasing from  $2^\circ$  to  $1/4^\circ$  and each color corresponds to a doubling of resolution. Cyan, brown, and magenta lines represent robust regression coefficients (Matlab *robustfit* command, see Street et al., 1988) among the 28 latitude bands for each doubling in resolution. Blue dashed lines show the robust regression line when all resolution doublings are taken into account. (b): Robust regression coefficients (colors) of  $C_t^{m+1}(\lambda) - C_t^m(\lambda)$  (left) and  $C_s^{m+1}(\lambda) - C_s^m(\lambda)$  (right) onto  $(\sigma^{m+1}(\lambda) - \sigma^m(\lambda)) / \sigma^A(\lambda)$ , within each frequency band (abscissae) and for each resolution change (ordinates). White squares indicate insignificant values. Interpretation example: the light red area in the left panel means that in the mesoscale range, and across the whole latitudinal range, increasing the model resolution from  $2^\circ$  to  $1^\circ$  is expected to yield a  $\sim 0.4$  increase in temporal correlations  $C_t$  in the regions where resolved SLA variances  $\sigma^m / \sigma^A$  increase by 100%.

Title Page

Abstract Introduction

Conclusions References

Tables Figures

◀ ▶

◀ ▶

Back Close

Full Screen / Esc

Printer-friendly Version

Interactive Discussion